The Influence of Plastic-Strain-Induced Anisotropy Modeled as Combined Isotropic-Kinematic Hardening in the Tension-Torsion Straining Problem (Ⅱ)

— Numerical Verifications with Experimental Measurements —

Yeong Sung Suh*

(*Received August 2, 1997*)

In order to examine the influence of plastic-strain-induced anisotropy (modeled as combined isotropic-kinematic hardening) on the stress response from the non-proportional straining in the tension-torsion tests, a strain-controlled calculation was performed and compared with experimental measurements. The back stress was visualized in the deviatoric stress space to determine the importance of the role of the kinematic component for the accurate prediction. The result revealed that a combination of isotropic and kinematic hardening, including the influence of the spin on the evolution of the back stress, leads to good qualitative agreement with experimental results. It was also shown that the kinematic component of the proposed hardening model plays significant role to predict the stress responses from the cornered strain path accurately.

Key Words: Plastic-Strain-Induced Anisotropy, Combined Isotropic-Kinematic Hardening, Back Stress, Tension-Torsion, Nonproportional Strain Path, Cornered Strain Path

1. Introduction

Most of the literature which attempts to formulate a constitutive relation for plastic-strain-induced anisotropy involving kinematic hardening at finite strain illustrate their numerical or analytical results by a simple shear problem. For the simple shear deformation which has long been used as a benchmark test for the constitutive modeling of the strain-induced anisotropy, torsion of thin-walled tubes was adequately used (see, for example, Paulun and Pecherski, 1987 ; Zbib and Aifantis, 1988). Torsion of a bar with solid circular cross-section was also used to avoid buckling in the case of large deformations (Van Der Giessen *et al.*, 1992). A tension-torsion test provides easily interpretable information for formulating constitutive relations in complicated situations.

In order to investigate the influence of plastic-strain-induced anisotropy, a two-dimensional numerical analysis of a tension-torsion test of a thin-walled tube has been carried out and compared with experimental data obtained from Cheng and Krempl (1989). Combined non-proportional tension-torsion straining involves a general interaction between the plastic strain-rate tensor and the back stress even at small strains. This therefore constitutes a convenient experimental procedure for investigating the structure of the plastic theory involved, in contrast to simple shear which involves general interactions only at finite strains, which restricts the generality of the test. The tension-torsion test shown in Fig. 1 offers an effective means to observe the evolution of stress response, and provides alternative relations for strain-induced anisotropy for a general range of variation of back stress and plastic strain

* Department of Mechanical Engineering, Hannam University, 133 Ojung-dong, Taeduk-gu, Taejon, Korea, 306-791

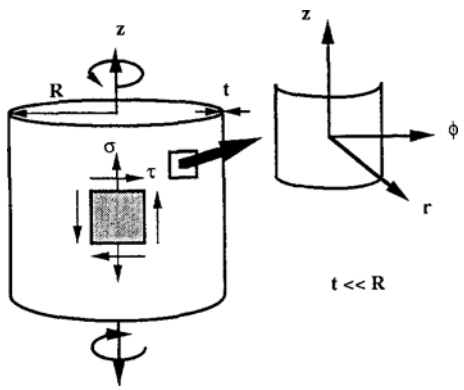

Fig. 1 Tension-torsion test of a thin-walled tube.

rate. The out-of-phase tension-torsion test as conducted by Lamba and Sidebottom (1978) can generate rotating bi-axial stress tensors which will be accompanied by only small material rotation, but are capable of producing large inclinations between back stress and plastic strain rate tensors at small strain. Using the structure of evolution of the back stress presented in part I, a numerical simulation of tension-torsion of a thin-walled cylinder was carried out. The results were compared with experimental data obtained from Cheng and Krempl (1991). Before this, the influence of plastic-strain-induced anisotropy on the axial stress development in fixed-end torsional straining, which was reported, for example, by Montheillet *et al.* (1984) and White (1988), and on the stress response from the straining along the path with a corner are presented.

2. Elastic-Plastic Constitutive Equations at Finite Strain

2.1 Basic constitutive equations

When the elastic strains are on the order of 10^{-3} (yield stress divided by elastic modulus magnitudes) so that plastic strains will generally dominate elastic strains, the Jaumann derivative of Kirchhoff stress, $\hat{\sigma}$, can be expressed as

$$\hat{\sigma} = L^e : (D - D^p) \tag{1}$$

with L^e as the elastic moduli which are obtained from the derivatives of the small deformation strain energy function. D is the rate of deformation and the superscript "p" denotes plastic. For combined isotropic-kinematic hardening model, the von-Mises yield condition takes the form

$$(\sigma' - \alpha) : (\sigma' - \alpha) = \frac{2}{3}\bar{\sigma}^2 \tag{2}$$

where σ' is the deviator of the stress, σ, $\bar{\sigma}$ the scalar representing the isotropic component of the current tensile yield stress. By assuming equivalence of the yield condition and the plastic potential, D^p can be written as

$$D^p = \sqrt{\frac{3}{2}}\,\dot{\bar{\varepsilon}}^p n \tag{3}$$

where $\dot{\bar{\varepsilon}}^p$ is the rate of effective plastic strain ($\dot{\bar{\varepsilon}}^p = \sqrt{\frac{2}{3}D^p : D^p}$), and n the unit normal to the yield surface expressed in Eq. (2) :

$$n = \sqrt{\frac{3}{2}}\,\frac{\sigma' - \alpha}{\bar{\sigma}} \tag{4}$$

Here the function $h(\alpha, D^p)$ in Eq. (2) of part I can be expressed in terms of the stress component $\sigma' - \alpha$ using Eq. (4) as

$$h(\alpha, D^p) = \frac{3}{2}\frac{\dot{\bar{\varepsilon}}^p}{\bar{\sigma}} h(\alpha, \sigma' - \alpha) \tag{5}$$

As described by Agah-Tehrani *et al.* (1987), the development of the consistency condition requires input concerning the updated yield condition which can be obtained by differentiating Eq. (2). With Eq. (5), the consistency equation takes the form

$$\hat{\sigma}' : (\sigma' - \alpha) - \frac{3}{2}\frac{\dot{\bar{\varepsilon}}^p}{\bar{\sigma}} h(\alpha, \sigma' - \alpha) : (\sigma' - \alpha) = \frac{2}{3}\bar{\sigma} H' \dot{\bar{\varepsilon}}^p \tag{6}$$

where

$$H'(\dot{\bar{\varepsilon}}^p) = \frac{d\bar{\sigma}}{d\bar{\varepsilon}^p} \tag{7}$$

is the isotropic hardening coefficient. It is convenient to express the consistency condition in the form

$$\dot{\bar{\varepsilon}}^p = \frac{(\sigma' - \alpha) : \hat{\sigma}'}{H\bar{\sigma}} \tag{8}$$

where H is the combined isotropic-kinematic hardening coefficient :

$$H = \frac{2}{3}H' + \frac{3}{2}\frac{(\sigma' - \alpha) : h(\alpha, \sigma' - \alpha)}{\bar{\sigma}^2} \tag{9}$$

Utilization of (6), (7) of part I, Eqs. (3) and (4), together with the consistency condition (8) and (9), leads to the following expression for D^p :

$$D^p=\frac{(n:\dot{\bar{\sigma}})n}{H} \tag{10}$$

with

$$H=\frac{2}{3}H'+c+\phi\,[n:\frac{1}{\sqrt{\alpha:\alpha}}(\alpha^2 n+n\alpha^2-2\alpha n\alpha)] \tag{11}$$

where H' and c are the isotropic and kinematic hardening modulus, respectively, and ϕ is a non-dimensional material dependent parameter which controls the contribution of the spin due to induced anisotropy. Note in Eq. (11) that the induced anisotropy terms come into play in the effective hardening modulus H.

Substitution of Eq. (10) into Eq. (1) and inversion of the resulting equation leads to the final structure of the rate-type constitutive relation

$$\dot{\bar{\sigma}}=L:D \tag{12}$$

where

$$L_{ijkl}=2\mu\left[\frac{1}{2}(\delta_{ik}\delta_{jl}+\delta_{il}\delta_{jk})+\frac{\nu}{1-2\nu}\delta_{ij}\delta_{kl}-\frac{\Theta n_{ij}n_{kl}}{\frac{H}{2\mu}+1}\right] \tag{13}$$

where $\Theta=1$ if $\bar{\sigma}=\bar{\sigma}_{max}$ and $\dot{\bar{\sigma}}>0$, and $\Theta=0$ if $\bar{\sigma}<\bar{\sigma}_{max}$ or $\dot{\bar{\sigma}}<0$. μ and ν are the shear modulus and Poisson's ratio of the material, respectively. In the computation, the parameter β expresses the proportion of the isotropic to kinematic hardening. This parameter is considered to be such that

$$H'=\beta H \tag{14}$$

$$c=\frac{2}{3}(1-\beta)H \tag{15}$$

where H' and c are computed from the slopes of the isotropic and kinematic hardening curves, respectively, and H from the uniaxial stress-strain curve. β is a material-dependent hardening parameter such that isotropic hardening corresponds to $\beta=1$, kinematic hardening to $\beta=0$.

2.2 Constitutive equations of tension-torsion of thin-walled tube

The combined isotropic-kinematic hardening theory was applied to the analysis of the stresses generated by deformation of a thin tube following a prescribed path in strain space. Assume that the tube wall is sufficiently thin so that the stress state is homogeneous, in which case the non-zero true stress components are

$$\sigma_{zz}=\sigma \text{ and } \sigma_{z\phi}=\sigma_{\phi z}=\tau \tag{16}$$

where z, ϕ and r indicate the axial, circumferential, and radial directions, respectively. At finite strain, McMeeking (1982) has obtained the non-zero components of $\dot{\bar{\sigma}}$, the Jaumann derivative of true stress :

$$\dot{\bar{\sigma}}_{zz}=\dot{\sigma}+\tau\dot{\gamma},\ \dot{\bar{\sigma}}_{\phi\phi}=-\tau\dot{\gamma},\ \dot{\bar{\sigma}}_{z\phi}=\dot{\tau}-\frac{\sigma\dot{\tau}}{2} \tag{17}$$

The elastic-plastic stress-strain relations are

$$D_{ij}=\frac{\dot{\bar{\sigma}}'_{ij}}{2\mu}+\frac{1}{9\chi}\delta_{ij}\,\dot{\bar{\sigma}}_{kk}+\frac{1}{H}n_{kl}\,\dot{\bar{\sigma}}_{kl}n_{ij} \tag{18}$$

where D is the rate of deformation, μ is the shear modulus, χ the bulk modulus, H is the effective hardening modulus expressed in Eq. (10), and n the unit normal to the yield surface. A superscipt prime indicates the deviator. Substitution of (17) into (18) yields :

$$D_{zz}=(\frac{1}{3\mu}+\frac{1}{9\chi})\dot{\sigma}+\frac{\dot{\gamma}\tau}{2\mu}+\frac{1}{H}[n_{zz}\dot{\sigma}-n_{z\phi}\dot{\gamma}\sigma+(n_{zz}-n_{\phi\phi})\dot{\gamma}\tau+2n_{z\phi}\dot{\tau}]n_{zz} \tag{19.a}$$

$$D_{z\phi}=(-\frac{\dot{\gamma}}{4\mu}\dot{\sigma}+\frac{1}{2\mu})\dot{\tau}+\frac{\dot{\gamma}\tau}{2\mu}+\frac{1}{H}[n_{zz}\dot{\sigma}-n_{z\phi}\dot{\gamma}\sigma+(n_{zz}-n_{\phi\phi})\dot{\gamma}\tau+2n_{z\phi}\dot{\tau}]n_{z\phi} \tag{19.b}$$

$$D_{\phi\phi}=-(\frac{1}{6\mu}-\frac{1}{9\chi})\dot{\sigma}-\frac{\dot{\gamma}\tau}{2\mu}+\frac{1}{H}[n_{zz}\dot{\sigma}-n_{z\phi}\dot{\gamma}\sigma+(n_{zz}-n_{\phi\phi})\dot{\gamma}\tau+2n_{z\phi}\dot{\tau}]n_{\phi\phi} \tag{19.c}$$

$$D_{rr}=-(\frac{1}{6\mu}-\frac{1}{9\chi})\dot{\sigma}+\frac{1}{H}[n_{zz}\dot{\sigma}-n_{z\phi}\dot{\gamma}\sigma+(n_{zz}-n_{\phi\phi})\dot{\gamma}\tau+2n_{z\phi}\dot{\tau}]n_{rr} \tag{19.d}$$

3. Numerical Implementation

Finding analytical solutions to the nonlinear ordinary differential equations derived in the former section is extremely complicated, and thus a explicit numerical method with very small incremental steps was carried out. For polygonal

paths, the size of the incremental step was 9.754×10^{-6}, which is smaller than the off-set strain, 1×10^{-4}. At the onset of each increment, the prescribed strain rates in the radial and circumferential directions are computed with enough iterations to ensure convergence. The integration algorithm used for this computation was given in Suh *et al.* (1991).

The material data used in the computation is based on experiments carried out by Cheng and Krempl (1991) in which a thin-walled tubular specimen was made of an Al/Mg aluminium alloy with initial yield stress of 52.5 MPa, Young's modulus E=68,653 MPa, and Poisson's ratio $\nu = 0.33$. The uniaxial hardening curve used in the computation was obtained from Cheng and Krempl (1991) where a complete set of the stress response data for the whole strain path was only available with the ALG4 specimen in which uniaxial stress-strain data were measured only up to 1% of strain. Thus, extrapolation was carried out from other specimens, ALC41 and ALG2, for which the data were measured up to 6% and 15% strain, respectively. Based on this, stress responses from various strain paths were computed by changing the parameters such as β and ϕ. Since the uniaxial stress-strain data are not so consistent for all the available specimens, the stress prediction should be analyzed in a qualitative sense.

4. Results and Discussion

4.1 Axial stress development in fixed-end torsional straining

Montheillet et al. (1984) have reported the axial stresses induced during the torsion testing of aluminium, copper and α-iron at temperatures between 20℃ and the hot working range. They measured induced, compressive axial force at low temperatures and small strains for all three metals. At high temperature and increased strain, the sign of the axial force was different for the single phase and two phase alloys. White (1988) also observed the same effect with 1100-O aluminium and 316 stainless steel specimens, Fig. 2. The magnitude of induced axial stress differs for

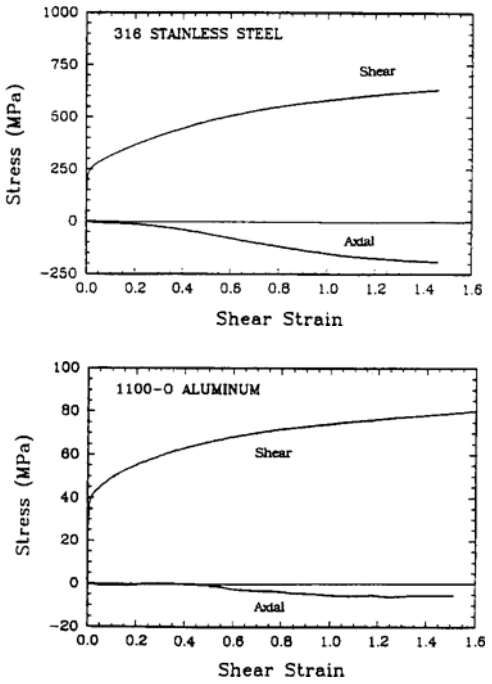

Fig. 2 Experimental results of the shear and axial stresses measured from a torsion test of type 316 stainless steel (above) and 1100-O aluminum (below) (White, 1988).

different materials. It seems that the material which has greater yield stress generates a larger magnitude of axial stress. Similar responses have also been predicted by the present numerical experiment by prescribing simple shear up to 6% of generalized shear strain with isotropic and kinematic hardening, Fig. 3. The magnitude of the yield stress of material used in the computation was between that of the two materials in Fig. 2. Figures 4 and 5 represent the generalized shear stress and the induced axial stress against shear strain, respectively. The former does not show any distinguishable variation under different β and ϕ, while the latter shows some variation. This is partly due to the incorporation of the Jaumann stress rate in the constitutive relation. When the magnitude of axial stress rate is zero, the axial Jaumann stress rate is reduced to $\tau\dot{\gamma}$, which is responsible for the predicted induced axial stress at finite strain. For a small strain formulation, this term does not appear. Since the order of $\dot{\sigma}\gamma$

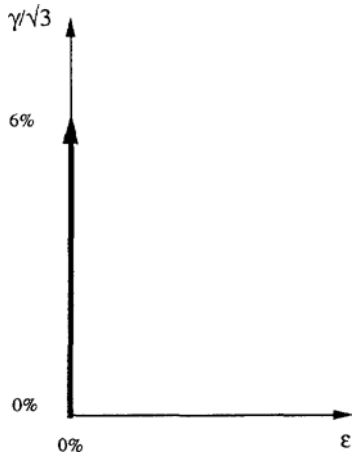

Fig. 3 Prescribed, generalized shear strain path up to 6%.

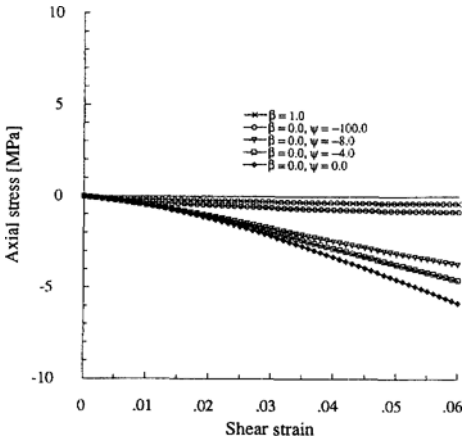

Fig. 5 Modification of Fig. 4 for the induced axial stress response.

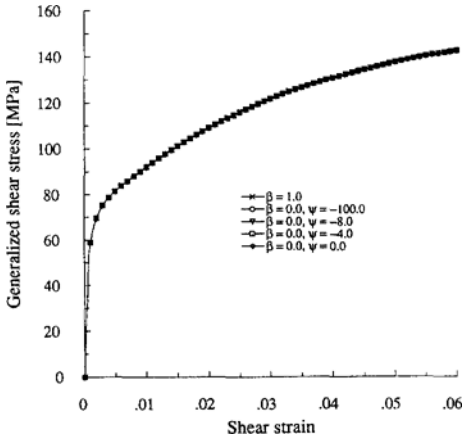

Fig. 4 Generalized shear stress response from the path prescribed in Fig. 3 under isotropic and kinematic hardening with various values of ψ.

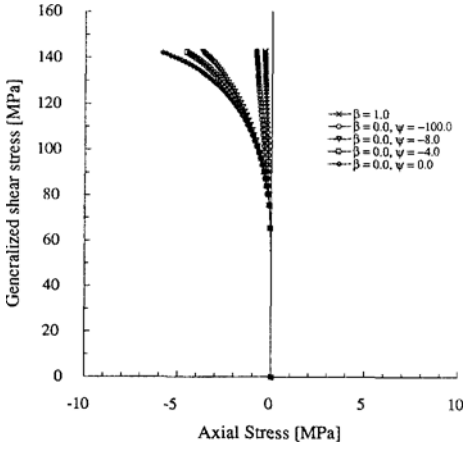

Fig. 6 Modification of Fig. 4 for the stress response in the axial stress-generalized shear stress space.

in the shear Jaumann stress rate is very small, this term hardly affects shear stress. This indicates why there are no discernable variations in Fig. 4. Terms such as $\tau\dot{\gamma}$ and $\sigma\dot{\gamma}$ do not appear in the small strain formulation. Numerical computations without the Jaumann stress rate generated no induced axial strain for both isotropic and kinematic hardening. The axially induced stress is more evident with kinematic hardening which includes the spin terms associated with induced anisotropy. This plays an important role when α and D^p develop non-coaxially. Figure 5, however, shows that kinematic hardening with no or little contribution of the spin associated with induced anisotropy leads to excessive induced axial stress in this range of deformation. Increasing the magnitude of ψ to 100 led to a reasonable amount of axial stress. As also indicated by Neale and Shrivastava (1985), isotropic hardening predicts small axial effects. Figure 6 shows the stress response in stress space. Note that the direction of the stress rate vector tends to recover that of the prescribed strain rate vector only with isotropic and kinematic hardening with $\psi = -100$. It is noted that the axially induced stress

can therefore be well predicted by controlling β and ϕ.

4.2 Straining along a path with a corner

The influence of plastic-strain-induced anisotropy in stress response to linear paths in strain space which intersects at a corner was examined. The direction of the stress vector is not tangential to the strain path immediately after the corner, but it becomes tangential to the strain path gradually as the strain point progresses along the prescribed linear path. To explain this, Ilyushin (1954) defined the "trace of delay" as the length of the strain path, after a change in strain path, required for the stress vector to once again become tangential to the strain trajectory.

Before the investigation of the corner effects for hardening material, computations with simpler assumptions were carried out to better understand stress behavior. Three cases with Young's moduli (E) equal to 68,653 MPa, 200,000 Mpa and 3,000,000 MPa for the elastic-perfectly plastic (non-strain-hardening) materials illustrated in Fig. 7 were analyzed. The prescribed strain history involved 1% axial prestrain, followed by a 90° corner in the axial-generalized shear stress space. The initial yield stress $Y_1=52.5$ MPa and Young's modulus $E=68,653$ MPa are typical values of Al/Mg aluminium alloy. By increasing Young's modulus to 3,000,000 MPa, nearly-perfectly-plastic material can be modeled for which D approximately equals to D^p. Since the axial strain is held constant immediately after the corner, $D_{zz}=0$. From the flow rule this leads to $\sigma_{zz}'=\frac{2}{3}\sigma_{zz}=0$, and hence $\sigma_{zz}=0$ as all the other normal stress components are. Therefore the axial stress will converge to zero unless the rotation effect due to shear strain is taken into account. Since there exists induced axial stress after the corner as explained in the previous section, the limiting stress will be slightly compressive. Figure 8 plots predicted axial and generalized shear stresses against the total length of the strain path. After the corner, the axial stress for the near-rigid case ($E=3,000,000$ MPa) drops very rapidly to zero while the elastic-plastic case shows a decreasing transition region due to elasticity. The shear stress shows the same pattern. This can be observed more clearly from Fig. 9, where stress responses for all three cases are plotted in stress space. Here, the von Mises yield surface can be represented by a quarter circle in axial stress-generalized shear stress space. The distance between adjacent symbols represents the increment of predicted stress for a fixed, prescribed strain increment. As the direction of plastic flow changes at the corner, the stress zips along the yield surface from the axial to shear direction due to the normality condition. In

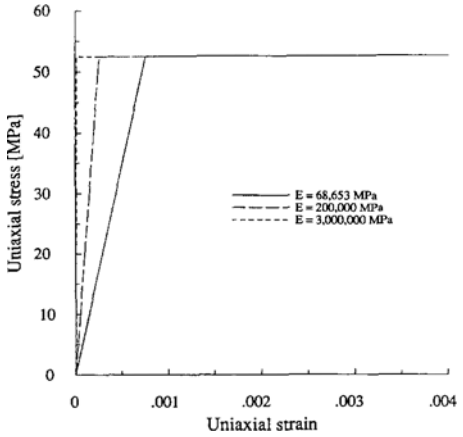

Fig. 7 Elastic-perfectly plastic, uniaxial stress-strain curve with different Young's moduli.

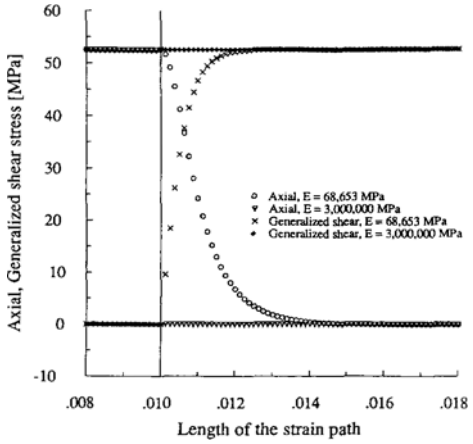

Fig. 8 Predicted axial and generalized shear stresses against the total length of the strain path for the elastic-plastic material ($E=68,653$ MPa) and the nearly-perfectly-plastic material case ($E=3,000,000$ MPa).

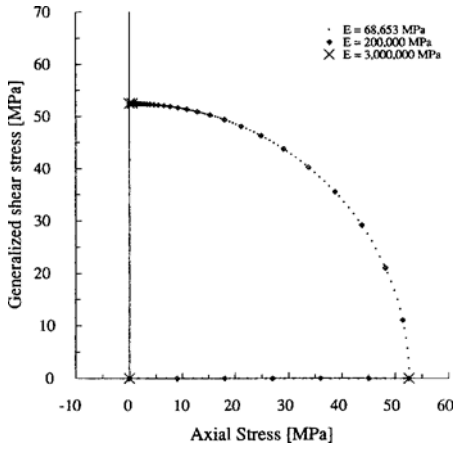

Fig. 9 Stress response in the axial stress-generalized shear stress space for various magnitudes of the Young's moduli.

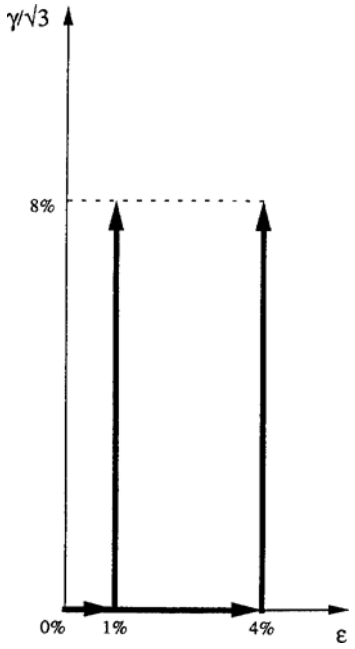

Fig. 10 Strain path with 1% and 4% axial prestrains respectively followed by 90° corners. Generalized shear strains are prescribed up to 8%.

the case of perfectly plastic material, the stress will jump traveling along the yield surface. This is well illustrated with higher Young's moduli such that the adjacent symbols are apart further in between the axes of the axial and the generalized shear stresses. Thus it can be deduced that the circular trajectory in stress space for elastic-plastic material is associated with the elasticity.

To examine corner effects with hardening, stress responses were computed for a strain path with 1% and 4% axial prestrains, respectively, followed by 90° corners as shown in Fig. 10. Before moving on to the results, the stress behavior around a corner under rigid-plastic assumption will be briefly analyzed. In Fig. 11, the two schematics indicate the change of direction of the stress rate before and immediately after the corner with isotropic and kinematic hardening, respectively, for rigid-plastic theory. With isotropic hardening, the stress rate immediately after the corner zips around the yield surface from the yield stress in tension. This is determined by the plastic flow law. When kinematic hardening is involved, since the flow rule contains back stress such that $D^p=\dot{\lambda}(\sigma'-\alpha)$, the saturation of the stress rate after the corner will be slower than that with isotropic hardening, and kinematic hardening will show some axial stress due to the prestrain.

Figure 12 shows variations of the axial (σ) and the generalized shear stresses ($\sqrt{3}\tau$) against the length of the strain path with isotropic, combined ($\beta=0.5$, $\psi=-100.0$, -4.0, 0.0), and kinematic hardening ($\beta=0.0$, $\psi=-100.0$) for elastic-plastic assumption. Before the corner, all the axial stress responses are coincident since only simple tension occurs, and thus symbols designating them are not to be confused with those of generalized shear stresses. Immediately after the corner, the axial stress decreases while the shear stress increases, both rapidly, and saturates eventually. The magnitude of axial stress is also decreased as that of β is increased. By increasing the magnitude of ψ, the saturated axial stresses become smaller since the spin associated with induced anisotropy is embedded in the effective hardening modulus as shown in Eq. (11). The same results are shown in stress space in Fig. 13. Since the length between symbols in the strain space is fixed, the size of increment in stress space indicates the rate of stress. Dense symbols in the later stage indicates that the stress is saturating. Since $\frac{d\tau}{d\gamma}=0$ when γ becomes

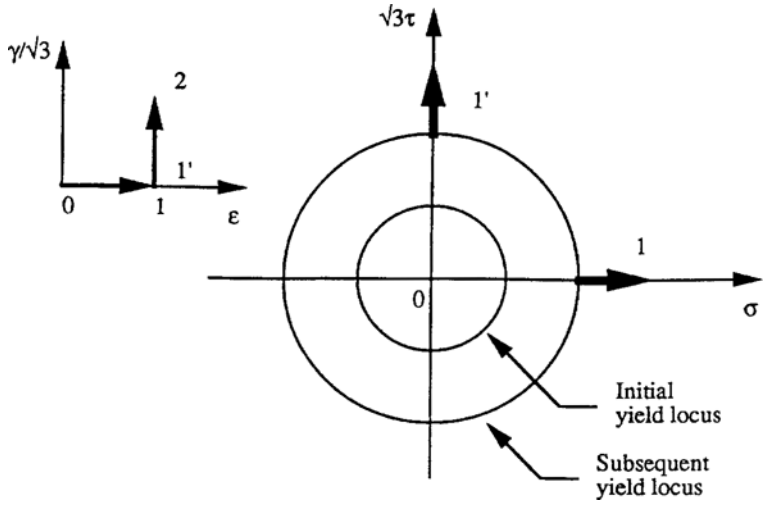

(a) Isotropic hardening

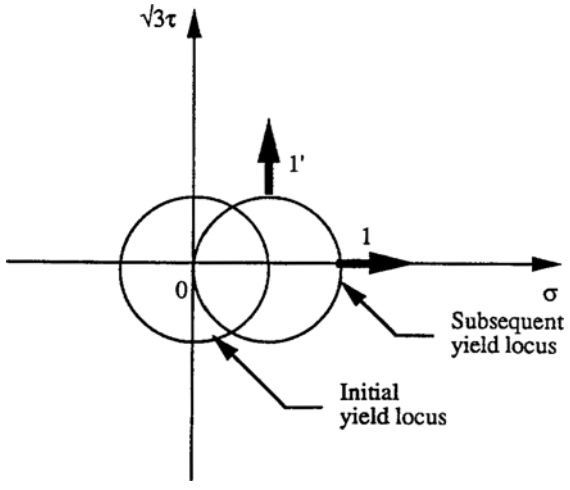

(b) Kinematic hardening

Fig. 11 Schematics indicating the change of direction of the stress rate before and immediately after the corner with isotropic and kinematic hardening assuming rigid-plastic theory.

large, shear stress will eventually saturate. In Fig. 13, only a larger magnitude of ψ led to the direction of the stress rate vector being tangential to that of the strain rate vector at later stages. Pure kinematic hardening ($\beta=0.0$) requires a longer strain path to recover the direction of prescribed strain. The stress responses with larger prestrain (4%) are plotted in Figs. 14 and 15. Similar to the previous case, isotropic hardening shows slightly compressive stress even with larger prestrain, which is not reasonable. By incorporating kinematic components, the effect of axial prestrain is well represented. According to Fig. 15, among combined isotropic-kinematic hardening, only the $\psi=-100.0$ case shows the direction of stress rate parallel to the prescribed shear strain rate vector. This indicates that, with appropriate values of β and ψ, experimental behavior can be correctly predicted.

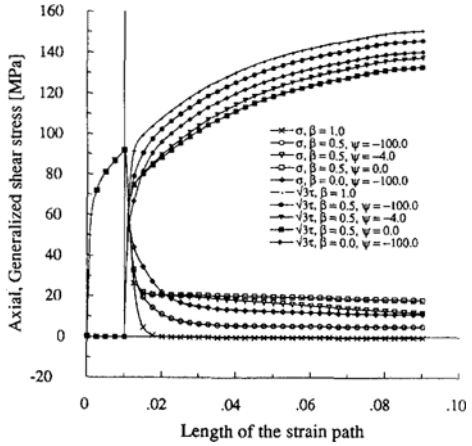

Fig. 12 Predicted axial and generalized shear stresses against the total length of the strain path for 1% axial prestrain followed by a 90 ° corner (Fig. 10) with isotropic, combined isotropic-kinematic ($\beta=0.5$, $\psi=-100.0$, -4.0 and 0.0) and kinematic hardening ($\psi=-100.0$).

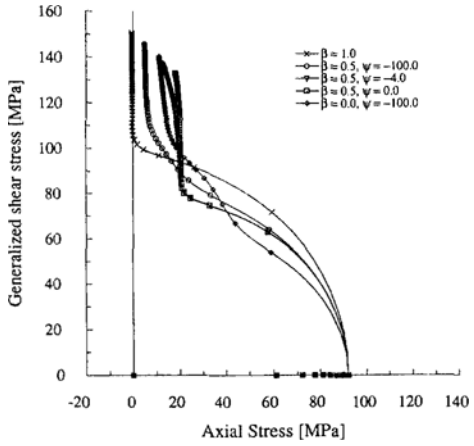

Fig. 13 Modification of Fig. 12 for stress response in the axial-generalized shear stress space.

4.3 Straining along the polygonal path

4.3.1. Evolution of the loading stress

The loading stress in this analysis is defined by the stress recorded in the stress space when the controlled strain reaches the corresponding yield surface probing station in the polygonally-prescribed strain path, shown in Fig. 2 of part Ⅰ. Following the polygonal strain path, loading stress response has been computed and monitored at each yield surface probing station. Figure 16

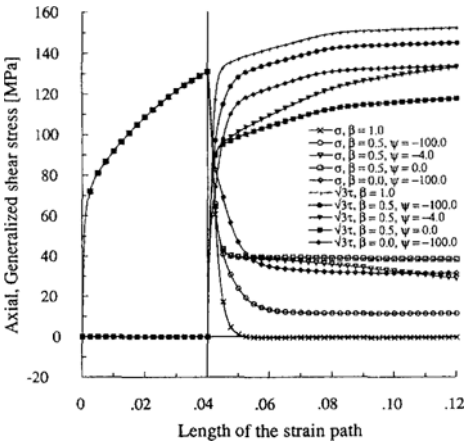

Fig. 14 Modification of Fig. 12 for 4% axial prestrain.

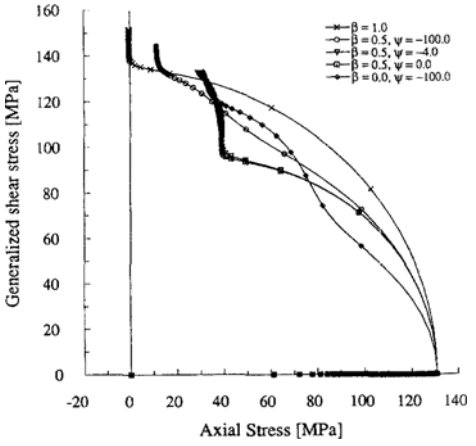

Fig. 15 Modification of Fig. 14 for stress response in the axial-generalized shear stress space.

shows predicted stresses under isotropic hardening ($\beta=1.0$) and kinematic hardening ($\beta=0.0$) with various values of ψ in comparison with experimental stress responses in $\sigma-\sqrt{3}\tau$ space. As previously mentioned, this comparison should be made in a qualitative sense due to material inconsistency. Experimental results were obtained from the ALF7 specimen, which has not gone through yield surface probing until station 14. For kinematic hardening, even with large magnitude ψ, stress responses are very much underpredicted except at earlier stages. The isotropic hardening case, on the contrary, overpredicts especially at later stages. This can partly be explained by the facts mentioned in two previous sections. In the

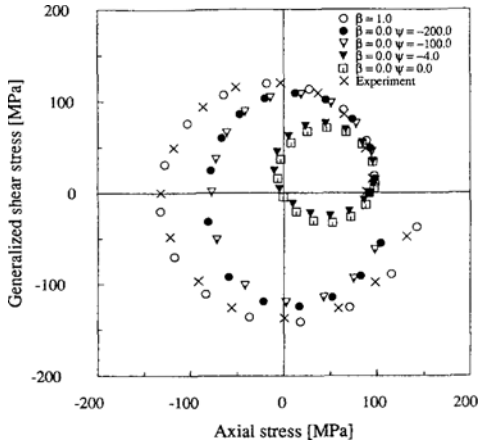

Fig. 16 Predicted stresses under isotropic hardening ($\beta=1.0$), kinematic hardening ($\beta=0.0$) with various values of ψ in comparison with experimental stress responses in the axial-generalized shear stress space.

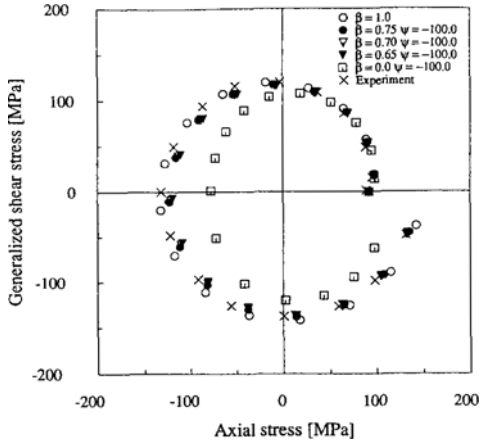

Fig. 17 Modification of Fig. 16 for $\beta=0.75$, 0.70 and 0.65 with $\psi=-100.0$.

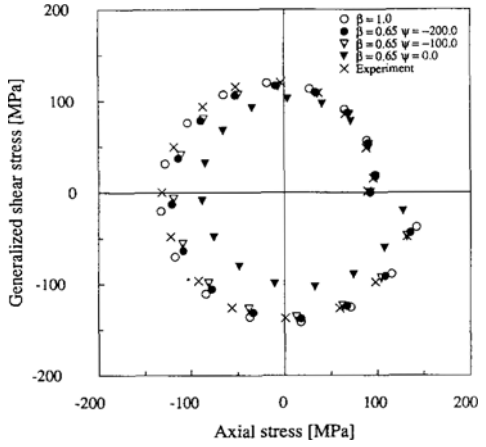

Fig. 18 Modification of Fig. 16 for $\beta=0.65$ with $\psi=-200.0$ and -100.0 and 0.0.

present path, torsionally induced axial stress and change of stress due to corners interact simultaneously, making the analysis complicated. It seems that predicted stresses with isotropic hardening show relatively good agreement with experiments. This may lead to an incorrect conclusion if the inconsistency of mechanical properties among different test specimens is not considered. Although obtained from the same material, almost all the specimens exhibit different stress-strain curves possibly due to initial anisotropy or inhomogeneity of the material. As previously mentioned, the stress-strain curve used in the computation was obtained from the specimen which was not the same as that used in the experiments. It is important, therefore, that the comparison should be made in a qualitative sense. By increasing the magnitude of ψ, the pattern of predicted stresses becomes closer to that of experimental stress responses at later stages. Figure 17 contains the results under hardening for various values of β with $\psi=-100.0$, and isotropic hardening. $\beta=0.65$, 0.70, 0.65 with $\psi=-100.0$ shows quite similar behavior and qualitatively matches the experimental stress pattern. Figure 18 contains the predicted stresses at a fixed value of β with different magnitudes of ψ, ψ larger than 100 shows good agreement, while no spin associated with induced anisotropy ($\psi=0$) was less successful. For all the cases, the largest disagreement with experimental data was observed immediately after the shear strain changed its direction. As yet the reason for this is not clear. It could perhaps be attributed to either the constitutive relation, which may not be able to cope with an abrupt change of the direction of shear strain, or an accumulation of plastic deformation due to experimental errors in probing for yield surfaces.

4.3.2. Evolution of the back stress

In the previous section, only the loading stress evolution was considered. With kinematic hardening, however, the evolution of back stress is

also important. Defining the back stress in stress space can differ according to the measure adopted. In this study the center of the yield locus in terms of the back stress was computed and compared with the centers of the yield loci obtained from the fitted circle by the procedure described in part I. It is important to recognize that the center of yield locus in the axial stress - generalized shear stress space cannot be identified directly as the components of the back stress as it is deviatoric. The correlation formulae expressing von Mises yield circle in the axial stress - generalized shear space have been derived in terms of the stress and the back stress in part Ⅰ. Figure 19 shows the evolution of the centers of experimental yield loci from the polygonal strain path depicted in Fig. 2 of part Ⅰ, obtained by a least squares fit procedure. Since the ALF7 specimen has not gone through yield surface probing until station 14, data from the ALG4 specimen, which generated a similar loading stress pattern as that of the ALF7, was selected. Three different cases are obtained from fittings based on 6, 10 and 12 component data sets over the nose geometry of the yield locus involving 3, 5, and 6 data sets, respectively, on each side of the axis of the prestraining direction. The evolution of the centers varies. However, note that the smaller data sets predict a larger kinematic component. It is clear that the smaller the number of data over the nose geometry, the smaller will be the curvature of the yield circle. Relatively reliable trajectories of the centers have been obtained by choosing the 12 data points. Based on this, the evolution of the centers computed from the numerical results was compared. The center of the computed yield locus is $(1.5\alpha_{zz}, \sqrt{3}\alpha_{z\phi})$, according to part Ⅰ. Figure 20 shows the evolution of centers of the yield loci with kinematic hardening for $\psi = -200.0$, -100.0, -4.0, and 0.0 in comparison with centers of the experimental yield loci computed by least squares fit. All numerical results differ significantly from the experimental data. This plot also suggesls that the magnitude of the back stress is increased when that of ψ increases. By increasing the isotropic component, *i. e.*, reducing the kinematic component, back stress magnitudes became closer to that of the ones from least squares fit, see Fig. 21. Figure 21 contains the results under various β with a fixed value of ψ. A larger portion of the isotropic component led to smaller magnitudes of the back stress. Selecting $\beta = 0.65$ as one of the better parameter sets to fit the experimental stress

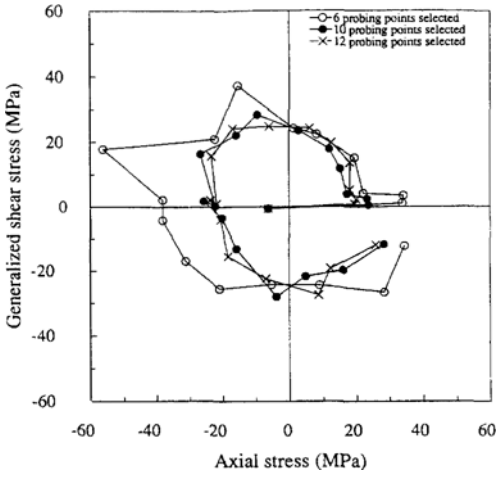

Fig. 19 Evolution of the centers of experimental yield loci for the polygonal strain path depicted in Fig. 2 of part Ⅰ, obtained by the least squares fit procedure. 6, 10 and 12 component data sets over the nose geometry of the yield locus, involving 3, 5, 6 data sets respectively on each side of the axis of the prestraining direction, have been selected.

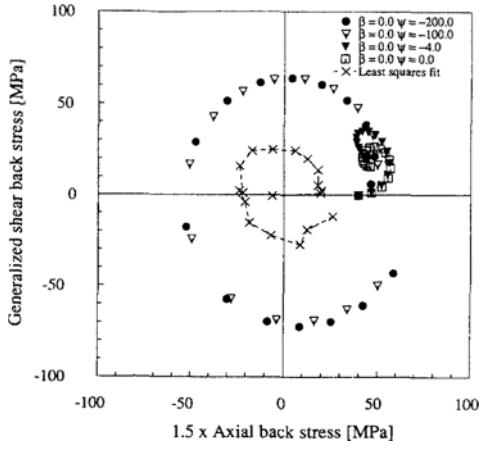

Fig. 20 Evolution of centers of the yield loci with kinematic hardening for $\psi = -200.0$, -100.0, -4.0, and 0.0 in comparison with centers of experimental yield loci computed by the least squares fit.

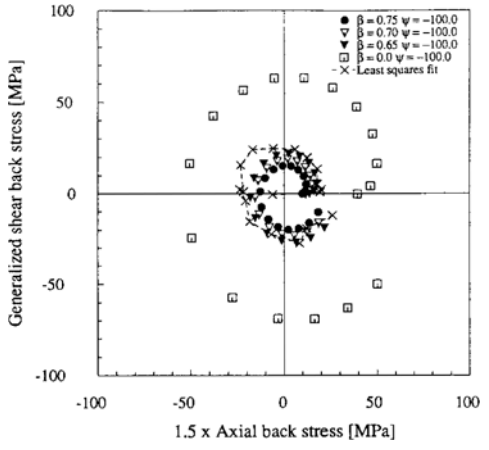

Fig. 21 Modification of Fig. 20 for $\beta=0.75$, 0.70, and 0.65 with $\psi=-100.0$.

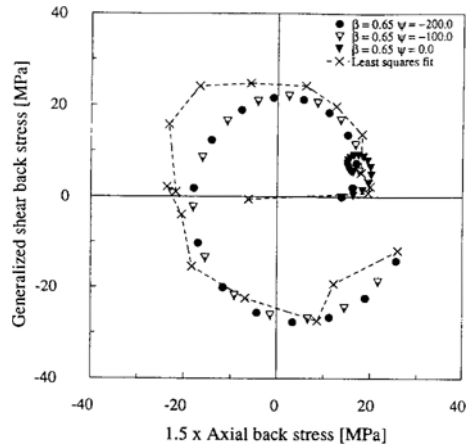

Fig. 22 Modification of Fig. 20 for $\beta=0.65$ with $\psi=-200.0$, -100.0 and 0.0.

pattern, from Figs. 18 and 21, the influence of ψ was examined in Fig. 22. No contribution of spin associated with induced anisotropy led to the evolution of the center far from that of the experiments. Although some sections differed from the experimental results, the magnitudes of ψ greater than or equal to 100 show relatively good agreement.

Comparing with experimental stress patterns, numerical prediction of both the loading stress and the center of the yield locus, expressed in terms of the back stress, indicates that inclusion of the plastic-strain-induced anisotropy into the constitutive modeling improves stress prediction of the tension-torsion test of a thin-walled tube.

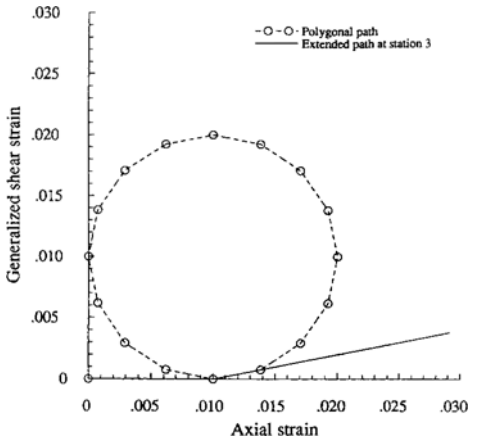

Fig. 23 Extended strain path at station 3 of the polygonal path in Fig. 2 in part I.

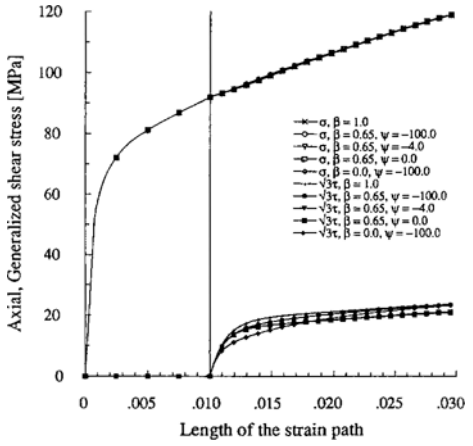

Fig. 24 Predicted axial and generalized shear stresses against the total length of the strain path for the extended path in Fig. 23.

4.3.3. Corner effect

To examine the corner effect which exists in the polygonal path, the extended straight paths at stations 3 and 7 of Fig. 2 in part I were prescribed respectively. Figure 23 shows the extended path emanating from station 3. The stress responses from this path are plotted in Figs. 24 and 25. Figure 24 indicates that the variation of generalized shear stress is more evident than that of axial stress. Figure 25 shows that, because of this shear stress variation, stress trajectories vary in the axial stress-generalized shear stress space under various values of β and ψ. Isotropic hardening and combined isotropic hardening of the

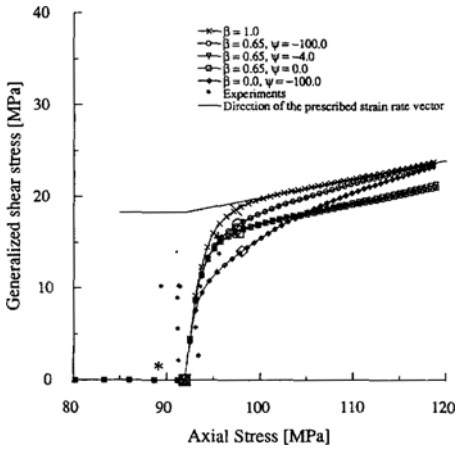

Fig. 25 Modification of Fig. 24 for stress response in the axial-generalized shear stress space. Bigger symbol denotes the data at the probing station.

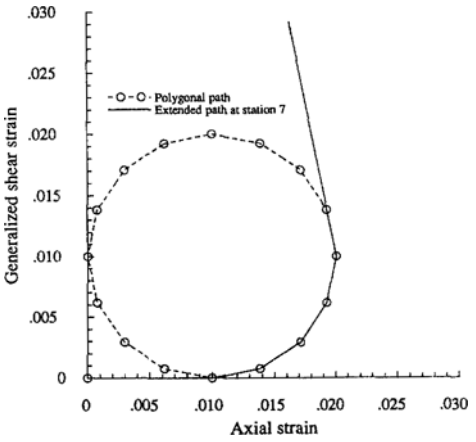

Fig. 26 Extended strain path at station 7 of the polygonal path in Fig. 2 in part Ⅰ.

$\beta=0.65$, $\psi=-100$ case, which recovers the direction of the strain rate fast, is close to experimental results. Pure kinematic hardening with $\psi=-100$ and combined hardening $\beta=0.65$ with $\psi=-4.0$ and 0.0 show less agreement at station 3. Similar patterns for the extended path emanating from station 7, Fig. 26, are shown in Figs. 27 and 28. Again, the $\beta=0.65$, $\psi=-100$ case shows good agreement with experimental results. Figure 28 indicates that the longer the strain path is traversed, the more drastic is the variation among the different parameter sets. Note that the direction of the stress rate vector with the polygonal path always lags behind that of the strain vector.

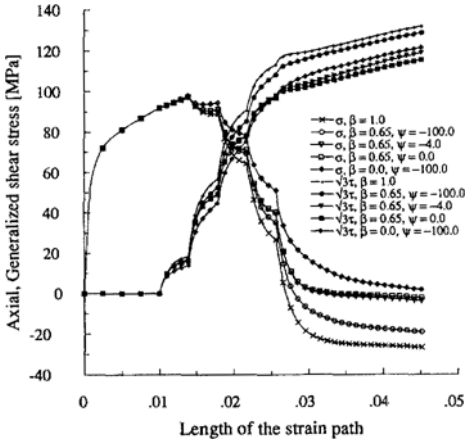

Fig. 27 Predicted axial and generalized shear stresses against the total length of the strain path for the extended path in Fig. 26.

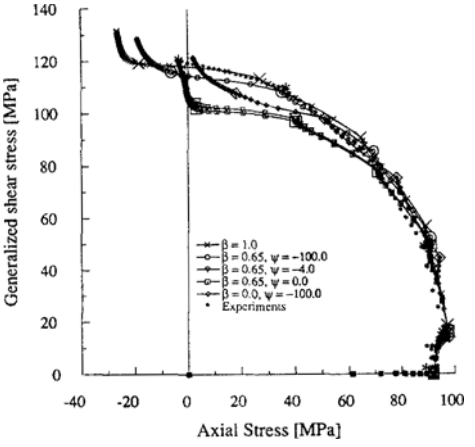

Fig. 28 Modification of Fig. 27 for stress response in the axial-generalized shear stress space. Bigger symbol denotes the data at the probing station.

5. Conclusion

The plastic-strain-induced anisotropy modeled as combined isotropic-kinematic hardening was effectively verified by the simulation of tension-torsion straining and its comparison with the corresponding experimental measurements. In contrast to the work done by Dafalias (1985) and Zbib and Aifantis (1988), who introduced plastic spin as a relative spin, and by Ning and Aifantis

(1997), who observed induced anisotropy in a level of grain and aggregate of polycrystalline, this work is significant in that the induced anisotropy derived from the isotropic tensor, which is a function of the back stress and the rate of plastic deformation (proposed by Agah-Tehrani *et al.*, 1987), was visualized numerically and verified with available experimental measurements. The major results obtained from this work are as follows :

(1) A program which computes the stress response from controlled finite strain path in the tension-torsion straining was successfully developed.

(2) Using the developed program, axially induced stress from the fixed-end torsion test was simulated in order to examine the role of plastic-strain induced anisotropy associated with kinematic hardening. Numerical findings indicated that only the finite deformation formulation of the constitutive equation and appropriate magnitude of plastic-strain-induced anisotropy can lead to the correct prediction of induced axial stress.

(3) Straining along a path with a corner has been analyzed in detail. It was shown that only the kinematic component with appropriate magnitude of plastic-strain-induced anisotropy can show traces of delay, which is an experimentally observed effect from the path with corner. Isotropic hardening showed trace of delay, although it is not so evident. However, it was shown that this is a result of the elasticity of the material, while with the kinematic hardening the back stress plays a major role in describing such a phenomenon.

(4) The center of the yield locus in terms of the back stress was computed and compared with the centers of the yield loci obtained from the fitted circle. Relatively reliable trajectories of the centers have been obtained by choosing the twelve data points. Based on this, the evolution of the centers computed from numerical results was compared. For the Al/Mg alloy tested, selecting $\beta = 0.65$ with the magnitudes of ψ greater than or equal to 100 show relatively good agreement. Compared to experimental stress patterns, numerical prediction of both the loading stress and the center of the yield locus, expressed in terms of the back stress, indicates that inclusion of the plastic-strain-induced anisotropy into the constitutive modeling improves stress prediction of the tension-torsion test of a thin-walled tube.

In this work, only the β and ψ, which are directly related with the first and the rotational terms in the full invariant form of the back stress evolution equation, were determined by parametric study and comparison with measurements. The structure of the spin associated with induced anisotropy in stress space still remains to be identified. By taking account of more terms in the full form of the invariant evolution equation, more accurate evaluation of the anisotropic hardening model could be achieved. To do so, more extensive and elaborate design of the test, and careful experiments to obtain consistent evolution of subsequent yield loci, are needed. This will be left as future work.

Acknowledgements

The author would like to thank Prof. E. Krempl of Rensselaer Polytechnic Institute and Dr. S. Cheng of Concurrent Technologies Corporation for providing valuable experimental data. The generous advice on this work by Dr. E. H. Lee, Emeritus Professor at both Rensselaer Polytechnic Institute and Stanford University, is gratefully acknowledged.

References

Agah-Tehrani, A., Lee, E. H., Mallett, R. L. and Onat, E. T., 1987, "The Theory of Elastic-Plastic Deformation at Finite Strain with Induced Anisotropy Modeled as Combined Isotropic-Kinematic Hardening," *J. Mech. Phys. Solids*, Vol. 35, pp. 519~539.

Cheng, S. and Krempl, E., 1991, "Experimental Determination of Strain-Induced Anisotropy During Nonproportional Straining of an Al/Mg Alloy at Room Temperature," *Int. J. Plasticity*, Vol. 7, pp. 827~846.

Dafalias, Y. F., 1985, "The Plastic Spin," *J.*

Appl. Mech., Vol. 52, pp. 865~871.

Ilyushin, A. A., 1954, "On the Relations between Stresses and Small Deformations in the Mechanics of Continuous Media," *Prikl. Mat. Mekh.*, Vol. 18, pp. 641~666.

Lamba, H. S. and Sidebottom, O. M., 1978, "Cyclic Plasticity for Nonproportional Paths : Part 1-Cyclic Hardening, Erasure of Memory, and Subsequent Strain Hardening Experiments," *J. Engng. Mat. Tech.*, Vol. 100, pp. 96~103.

McMeeking, R. M., 1982, "The Finite Strain Tension Torsion Test of a Thin-Walled Tube of Elastic-Plastic Material," *Int. J. Solids Structures*, Vol. 18, pp. 199~204.

Montheillet, F., Cohen, M. and Jonas, J. J., 1984, "Axial Stresses and Texture Development during the Torsion Testing of Al, Cu, and a-Fe," *Acta Metall.*, Vol. 22, pp. 2077~2089.

Neale, K. W. and Shrivastava, S. C., 1985, "Finite Elastic-Plastic Torsion of a Circular Bar," Eng. Fract. Mech. ., Vol. 21, pp. 747~754.

Ning, J. and Aifantis, E. C., 1997, "Anisotropic Yield and Plastic Flow of Polycrystalline Solids," *Int. J. Plasticity*, Vol. 12, pp. 1221~1240.

Paulun, J. E. and Pecherski, R. B., 1987, "On the Application of the Plastic Spin Concept for the Description of Anisotropic Hardening in Finite Deformation Plasticity," *Int. J. Plasticity*, Vol. 3, pp. 303~314.

Van Der Giessen, E., Wu, P. D., and Neale, K. W., 1992, "On the Effect of Plastic Spin on Large Strain Elastic-Plastic Torsion of Solid Bars," *Int. J. Plasticity*, Vol. 8, pp. 773~801.

White, C. S., 1988, "A Combined Isotropic-Kinematic Hardening Model for Large Deformation Metal Plasticity," *Final Report, MTL TR 88-46*, U. S. Army Material Technology Laboratory.

Zbib, H. M. and Aifantis, E. C., 1988, "On the Concept of Relative and Plastic Spins and its Implications to Large Deformation Theories. Part Ⅱ : Anisotropic Hardening Plasticity," *Acta Mech.*, Vol. 75, pp. 35~56.